Electronic supplementary materials

For https://doi.org/10.1631/jzus.A2500370

Effect of varying strain rates on the local mechanical properties of aluminum alloy welded joints

Chen LIU[1*], Yansong WANG[1*], Chenmeng WANG[1,2], Hu Zhou[1], Yuchen YANG[1,3], Bangping GU[1], Shibin SUN[1], Long PAN[4], Feilong LIU[5], Guanhua XU[6,7], Chuanxiao YANG[1]

[1]*Logistics Engineering College, Shanghai Maritime University, Shanghai 201306, China*
[2]*College of Mechanical Engineering, Donghua University, Shanghai 201620, China*
[3]*School of Mechanical and Power Engineering, East China University of Science and Technology, Shanghai 200237, China*
[4]*School of Mechanical Engineering, Nanjing Institute of Technology, Nanjing 211167, China*
[5]*School of Materials Science and Engineering, Shanghai Jiao Tong University, Shanghai 200240, China*
[6]*State Key Laboratory of Fluid Power and Mechatronic Systems, School of Mechanical Engineering, Zhejiang University, Hangzhou 310058, China*
[7]*Zhejiang Key Laboratory of Additive Manufacturing Technology and Equipment, School of Mechanical Engineering, Zhejiang University, Hangzhou 310058, China*

S1 Experimental materials and methods

S1.1 Specimen preparation

The specimens were prepared as illustrated in Fig. S1. In accordance with GB/T228.1-2021 (GB/T228.1-2021), the design and processing of standard dumbbell-shaped specimens are delineated. The geometric dimensions are specified as 3 mm thickness and 25 mm width. The weld seam was to be arranged in strict symmetry along the specimen center line. The AA5052 aluminum alloy and its welding wire are utilised for the welding process, and their chemical compositions are detailed in

Table **S1**.

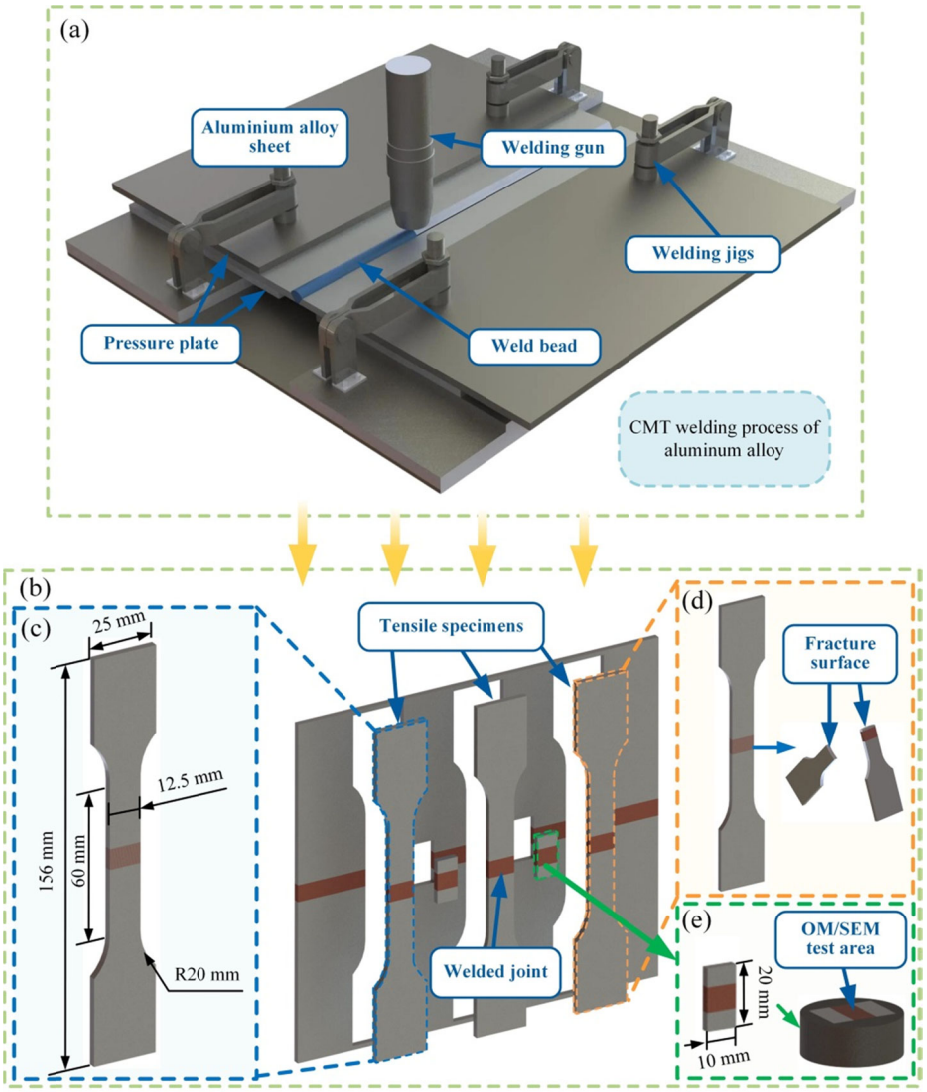

Fig. S1 Specimen preparation: (a) Welding process; (b) Schematic diagram of tensile specimens cutting; (c) Dimensions of tensile specimen; (d) Schematic diagram of fracture morphology testing; (e) OM/SEM specimen.

Table S1 Chemical Components of AA5052 aluminum alloy and ER5356 welding wire.

Materials	Si	Fe	Mn	Mg	Cr	Zn	Al
AA5052	0.146	0.247	0.027	2.454	0.266	0.027	Bal.
ER5356	0.25	0.4	0.2	5.5	0.2	0.1	Bal.

S1.2 Residual stress test by hole-drilling method

According to GB/T 31310-2014 (GB/T 31310-2014), the residual stress of AA5052 aluminum alloy specimens was measured using the hole-drilling method, with specialized drilling equipment. The configuration of the test system and its operational principles are illustrated in Fig. S2. Before testing, the specimens required systematic surface preparation. ATJ120-1.5 strain gauges were selected and installed using a rapid-curing adhesive. During installation, it is imperative to ensure the strain grid is precisely positioned by applying uniform pressure through a PTFE-coated film. The drilling operations were performed using the ZDL-II hole-drilling method, which was equipped with a diamond twist drill bit. A positioning fixture was utilized to ensure the drilling axis was aligned with the normal direction of the measurement point, thereby facilitating precise alignment. Before drilling, the cutting depth was precisely controlled via a locking mechanism. The positioning and connection of the strain rosette must strictly adhere to the prescribed procedures, as illustrated in Fig. S2.

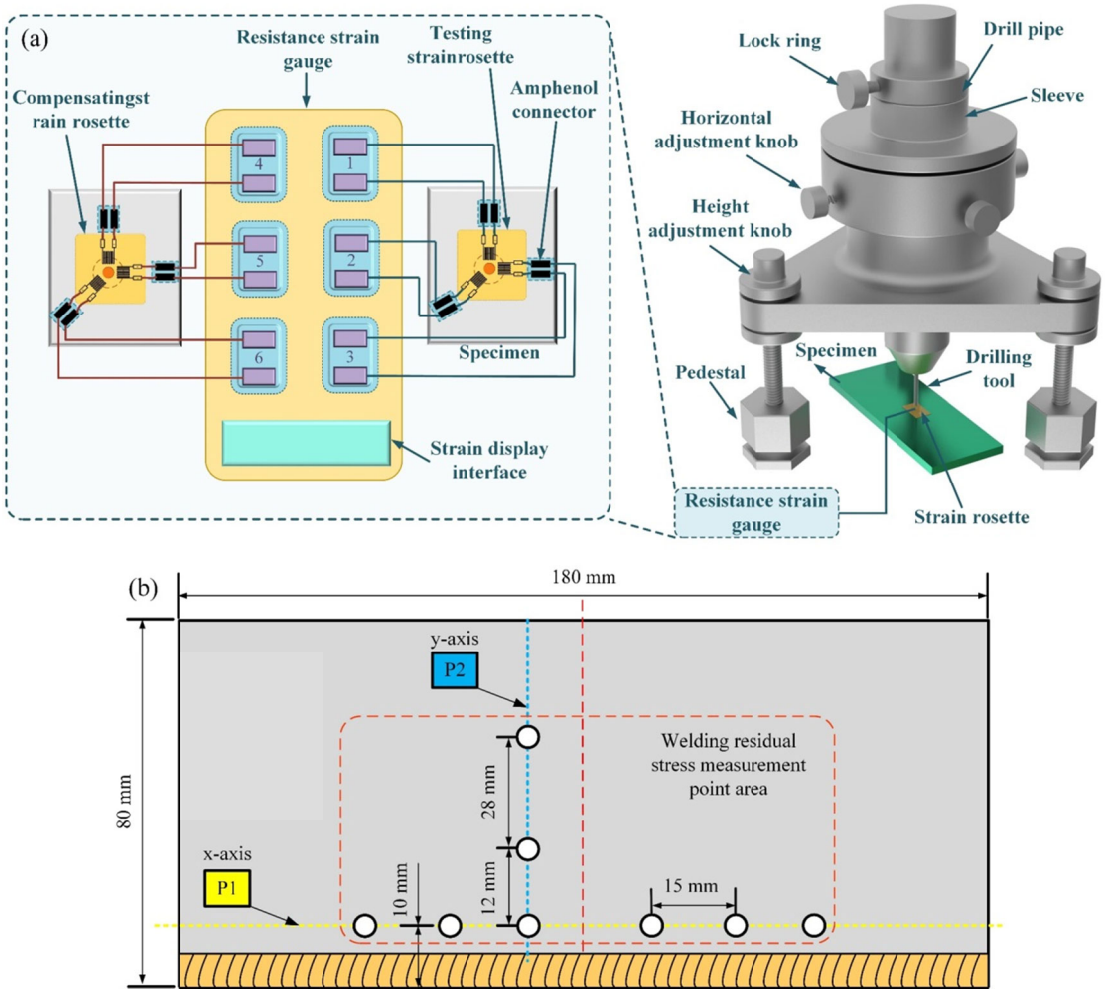

Fig. S2 Residual stress measurement based on the hole-drilling method: (a) Hole-drilling residual stress measurement equipment; (b) Residual stress measurement point distribution.

The strain measurement system utilizes a YE2538 multi-channel static strain gauge, which enables synchronous collection of strain release in three directions. The residual stresses were calculated by the radial strains ε_1, ε_2, and ε_3, measured by the strain gage, in conjunction with the material modulus of elasticity E and Poisson's ratio v. The following equations can derive residual stress in the x and y-directions:

$$\begin{cases} \sigma_x = \dfrac{(\mathrm{A}+\mathrm{B})}{4\mathrm{AB}}\left(\Delta\varepsilon_1 + \dfrac{(\mathrm{B}-\mathrm{A})}{(\mathrm{A}+\mathrm{B})}\Delta\varepsilon_3\right) \\ \sigma_y = \dfrac{(\mathrm{A}+\mathrm{B})}{4\mathrm{AB}}\left(\Delta\varepsilon_3 + \dfrac{(\mathrm{B}-\mathrm{A})}{(\mathrm{A}+\mathrm{B})}\Delta\varepsilon_1\right) \end{cases} \tag{S1}$$

S1.3 Characterization methods

In the present study, the GX53 inverted metallographic microscope was utilized to systematically observe the microstructure of the WM, HAZ, and BM. The polished specimens undergo chemical etching. The specimens were treated with Keller's reagent (composition: HF: HCl: HNO_3: H_2O = 1:1.5:2.5:95) by etching for 120 s, followed immediately by ultrasonic cleaning with anhydrous ethanol. To further reveal microstructural details, high-resolution imaging was performed using Scanning Electron Microscopy (SEM), with a focus on key microstructural parameters, including precipitation phase morphology and grain boundary characteristics. The phase composition of the welded joint was obtained using Cu-Kα radiation (1.5406 Å) X-ray diffraction (XRD, D8 Advance, Bruker, Germany).

The LCW-1K Vickers hardness testing system was used to characterize the surface microhardness

distribution of the welded joints. To ensure test accuracy, the specimens underwent a standardized preparation process. First, a flat surface was obtained by grinding and polishing in steps, and the final polishing stage was performed with a 0.05 μm silica suspension until the surface reached a mirror-like finish. Three parallel test paths were meticulously designed in the target area, spaced 0.2 mm apart. A total of 60 equally spaced test points were established in each path, with the interval between neighboring points being 0.2 mm. The experiment was conducted with a 300 g test force and a holding time of 10 s, and the test trajectory was planned and configured as shown in Fig. S3.

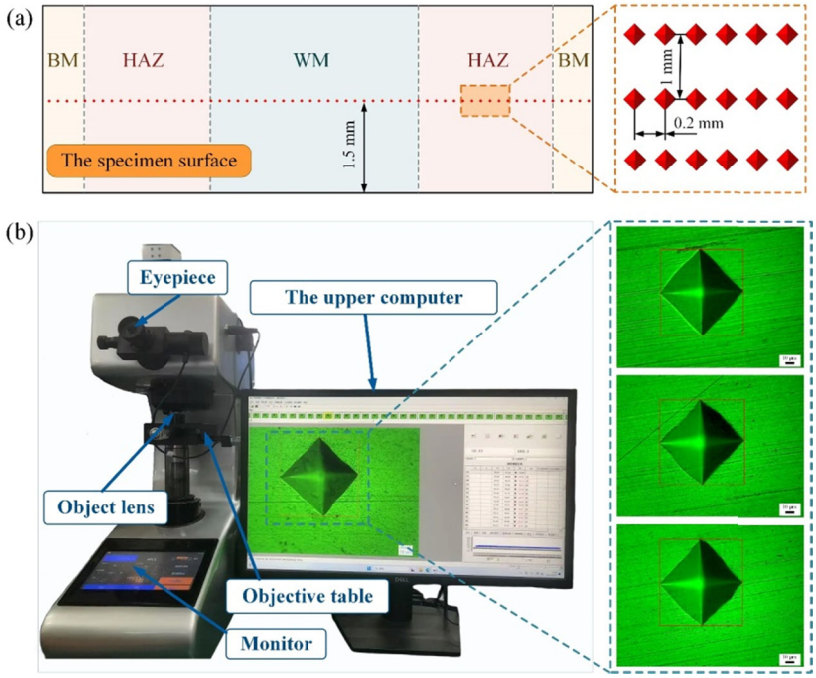

Fig. S3 Schematic diagram of microhardness measurement: (a) Microhardness measurement of the specimens; (b) Microhardness results.

S1.4 Tensile test and DIC testing method

The specimen preparation stage of the experiment involved the use of CNC electrical discharge wire-cutting technology (model DK7735), as illustrated in Fig. S1. Precision machining was performed in accordance with the specified geometric parameters. The tensile test was performed using a four-level loading rate scheme: 0.3 mm/min, 3 mm/min, 30 mm/min, and 60 mm/min, corresponding to strain rates of 1×10^{-4} s^{-1}, 1×10^{-3} s^{-1}, 1×10^{-2} s^{-1}, and 2×10^{-2} s^{-1}. The hierarchical loading scheme has been demonstrated to provide a systematic approach to characterizing the mechanical response of welded joints under varying deformation rates. The lowest loading rate is intended to simulate quasi-static conditions, while the highest loading rate is used to study dynamic deformation behavior.

As demonstrated in Fig. S4, the XTDIC 3D optical measurement system, in conjunction with DIC technology, was utilized in the present study. The process of preparing the scattering pattern is carried out strictly in accordance with a standardized procedure. Initially, the specimen is meticulously sanded with 600# sandpaper, followed by ultrasonic cleaning with anhydrous ethanol and drying. Thereafter, a white matte primer is applied by hand-spraying uniformly and subsequently cured at room temperature for 30 min. Ultimately, black scattering spots are formed on the surface of the white primer via atomized spraying to ensure the scattering pattern meets the requirements for deformation measurement accuracy. The DIC system has been developed to adjust the sampling frequency synchronously to 2000 ms, 1000 ms, 50 ms, and 20 ms to achieve dynamic tracking of the deformation process.

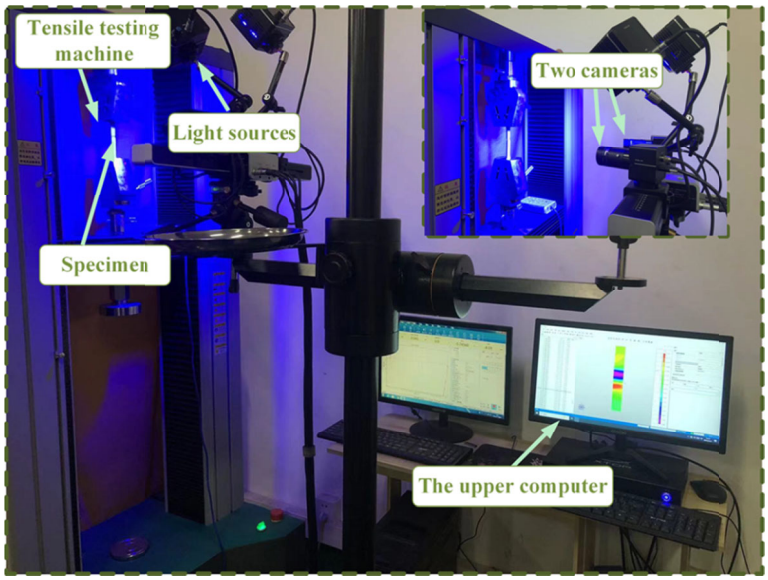

Fig. S4 Schematic diagram of the DIC test system.

S1.5 Introduction to fitting equations for stress-strain relationships

The Ramberg-Osgood equation is a valuable tool for characterizing the smooth transition properties of materials within the elastic-plastic transition interval (Ye et al., 2025; Basan et al., 2017). Its simple form and clear physical meaning make it particularly well-suited for ductile materials that exhibit significant strain-hardening behavior. The plastic behavior of AA5052 aluminum alloy can be characterized in practical terms by the strength coefficient K and the hardening index n. These parameters are well-suited for the parametric characterization and comparison of local constitutive relations in different regions (WM, HAZ, BM). For elastic-plastic materials commonly found in engineering, researchers often use the power function-type constitutive relation proposed by Ramberg et al., whose general expression is as follows (Basan et al., 2017):

$$\varepsilon = \varepsilon_e + \varepsilon_p = \frac{\sigma}{E} + \left(\frac{\sigma}{K}\right)^{\frac{1}{n}} \tag{S2}$$

In Eq. (S2), where ε denotes the engineering true strain characterized by logarithmic strain, ε_e and ε_p correspond to the true strain components in the elastic deformation stage and the plastic flow stage, respectively, σ is the actual stress parameter, E is the elastic modulus of the material, K is the strength coefficient reflecting the yield characteristics of the material, and n is the power exponent describing the strain hardening behavior. Based on the whole stress-strain curve obtained from the unidirectional tensile experiment, this study nonlinearly fits the K to the inverse of the hardening exponent ($1/n$). The parameter calibration process strictly follows the basic assumptions of the Hollomon hardening model (Peng et al., 2018) to ensure the reasonableness of the material of intrinsic relationship.

The first term of the equal sign in Eq. (S2) characterizes the strain response of the material during the elastic deformation phase and is calculated using Hooke's law:

$$\varepsilon_e = \frac{\sigma}{E} \tag{S3}$$

The second term on the right-hand side of Eq. (S2) denotes the plastic strain (Leitão et al., 2012):

$$\varepsilon_p = \left(\frac{\sigma}{K}\right)^{\frac{1}{n}} \tag{S4}$$

$$\sigma = K\varepsilon_p^n \tag{S5}$$

The double-logarithmic equation was obtained by taking the logarithm of Eq. (S5) (Gu et al., 2025);

$$\lg\sigma = n\lg\varepsilon_p + \lg K \tag{S6}$$

When the material lacks a yield plateau, the value of K can be fitted using the following formula.

$$K = \frac{\sigma_0}{\varepsilon_{0.2}^n} \tag{S7}$$

In the equation, $\varepsilon_{0.2}$ represents the yield stress corresponding to the proper offset plastic strain of σ_0.

$$\frac{E\varepsilon}{\sigma_0} = \frac{\sigma}{\sigma_0} + \alpha\left(\frac{\sigma}{\sigma_0}\right)^N \tag{S8}$$

In the equation, $N=1/n$, and is the dimensionless material constant.

By comparing the plastic part of the strain given in Eq. (S2), and (S8), the true plastic strain can be expressed as

$$\varepsilon_p = \frac{\alpha\sigma_0}{E}\left(\frac{\sigma}{\sigma_0}\right)^N \tag{S9}$$

The transformed Ramberg-Osgood equation was presented as follows:

$$\varepsilon = \varepsilon_e + \varepsilon_p = \frac{\sigma}{E} + \left(\frac{\sigma}{K}\right)^{\frac{1}{n}} = \frac{\sigma}{E} + \frac{\alpha\sigma_0}{E}\left(\frac{\sigma}{\sigma_0}\right)^N \tag{S10}$$

Conventional engineering stress-strain representations were challenging to employ accurately to describe the true mechanical behavior of materials during the plastic flow stage, and their limitations primarily stem from the continuous evolution of the specimen geometry. As the specimen's cross-sectional area progressively reduces during unidirectional stretching, particularly after necking, a substantial three-way stress nonuniformity becomes evident within the material. This geometrical hardening effect gives rise to a significant deviation in stress calculation, as based on the original cross-sectional area. Consequently, it becomes imperative to normalize the mechanical response through the utilization of true stress and true strain parameters, thereby facilitating the construction of a stress-strain curve that accurately reflects the intrinsic hardening behavior of the material.

The hardening curve displays a distinct power-law relationship, which was a hallmark of the steady-state deformation interval. By intercepting the data within this interval and conducting a thorough analysis, the strength factor K and the hardening index n of the material can be ascertained. These two fundamental parameters exhibit a strong correlation with the tensile strength of the material. Parameter n is indicative of the uniformity of strain distribution during plastic deformation, and it is established that a larger value corresponds to higher strain transfer efficiency. This, in turn, facilitates homogeneous deformation through lattice rotation and dislocation rearrangement. Parameter K, meanwhile, is associated with the material of resistance to plastic deformation, a property that directly influences load distribution during the forming process.

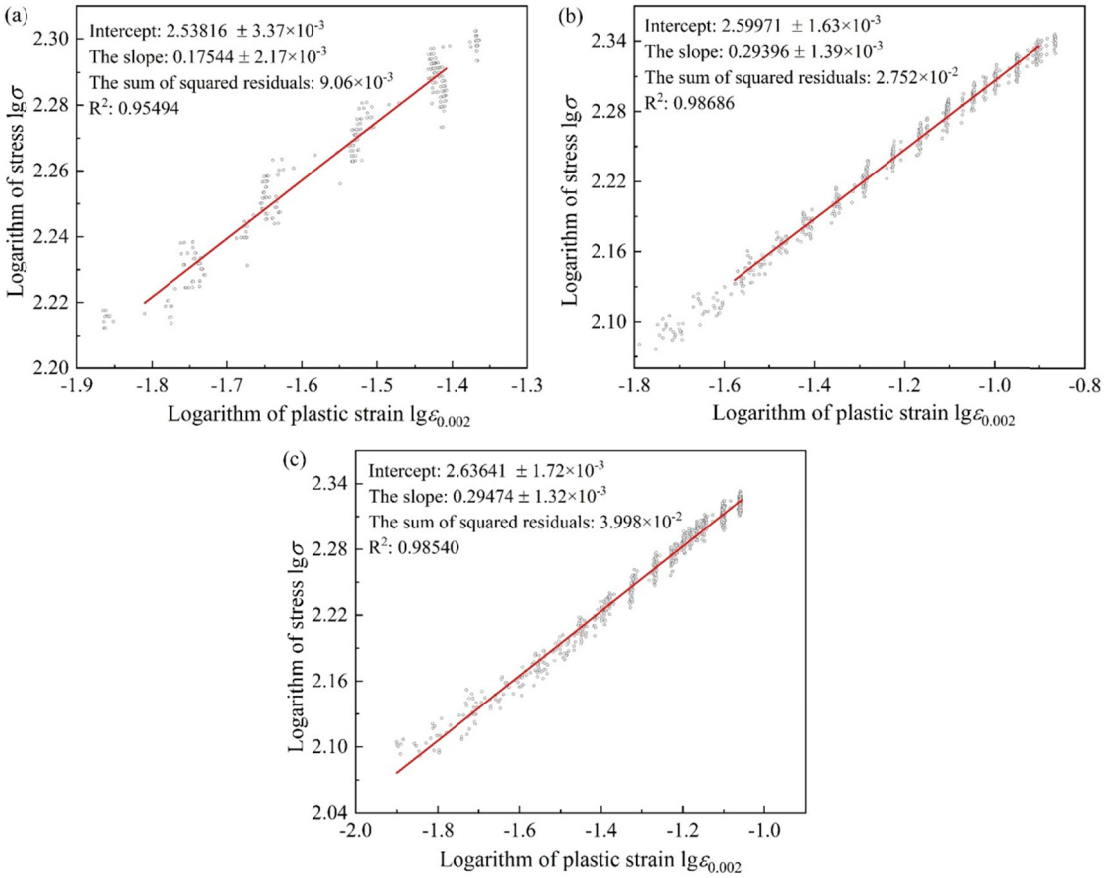

Fig. S5 Plasticity model fitting of aluminum alloy welding specimens: (a) BM; (b) HAZ; (c) WM.

As shown in Fig. S5, the hardening parameters obtained experimentally across the various regions (BM, HAZ, WM) of aluminum alloy welded joints are directly associated with the mechanical properties and the quality of the welded structures.

The Considère criterion compares the hardening rate (derivative of the stress-strain curve) with the current stress level by analyzing the geometric characteristics of the actual stress-strain curve (Patwardhan et al., 2019). When the hardening rate curve intersects the stress-strain curve, it indicates that the material of ability to resist local deformation has been exceeded, preventing uniform plastic flow. At this point, the deformation will concentrate in a localized region, indicating necking. The ultimate tensile strength of the material is defined as the stress at the critical state, where the hardening rate decays to match the current strain rate. According to the Considère criterion, the tensile strength can be defined as the stress when the processing hardening index is equal to the ultimate true strain (Kang et al., 2014):

$$\sigma_t = K\left(\varepsilon_t\right)^n = Kn^n \tag{S11}$$

The tensile strength of the local region of the aluminum alloy welded joint was fitted using Eq. (S11).

S2 Simulation of Aluminum alloy welding

S2.1 Finite element modelling and meshing

In this section, the residual stress distribution of welded joints is studied using a welding model of AA5052 aluminum alloy. A simulation analysis is performed using ABAQUS software. Initially, the thermal analysis for the welding model is calculated. Subsequently, the temperature field is imported into the predefined field of the welding stress field. This enables coupling the welding temperature and welding stress fields and subsequently determining the final residual stress distribution. The specific process is illustrated in Fig. S6.

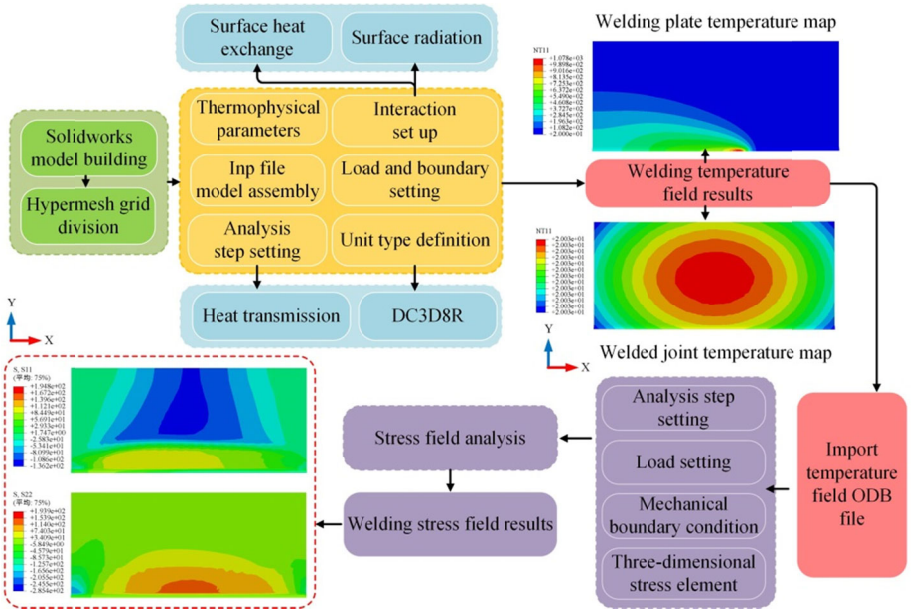

Fig. S6 Diagram of welding simulation process.

The present study employs SolidWorks software to perform 3D geometric modelling, utilizing the actual geometric characteristics of the BM of the welding test. Hypermesh completes the finite element meshing. To enhance computational efficiency, a semi-symmetric modelling scheme has been adopted. In the numerical analysis, the welded structure is constructed from a single side. The key dimensional parameters of the overall model are 180 mm in length, 80 mm in width, and 3 mm in plate thickness. The weld seam area is locally refined in the geometric model of the AA5052 aluminum alloy, based on the WM of actual forming characteristics. In the WM and its HAZ, fine discretization is implemented, and the minimum cell size is controlled to be 1 mm^3, as shown in Fig. S7. To accurately capture the physical field characteristics in the region where the temperature gradient changes drastically, the distal region of the BM has a sparse mesh transition. This transition enables a smooth change in mesh density from 1 to 4 mm via the dimensional gradient law. This grid distribution strategy effectively reduces the total number of cells and nodes to 20970 and 25663, respectively, while guaranteeing the computational accuracy. This improvement in computational efficiency is a key result of this strategy.

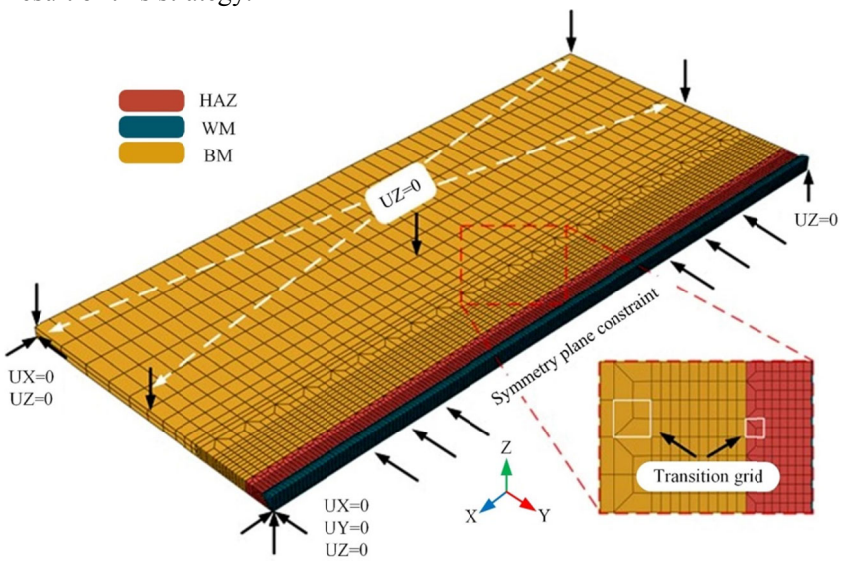

Fig. S7 Mesh division and constraint setting of the welding model.

As shown in Fig. S8, the double-ellipsoid volumetric heat-source model (Wang et al., 2022) and the welding temperature field diagram are presented. The model, composed of two 1/4 ellipsoids arranged

front-to-back, better simulates the molten pool shape and temperature distribution during welding.

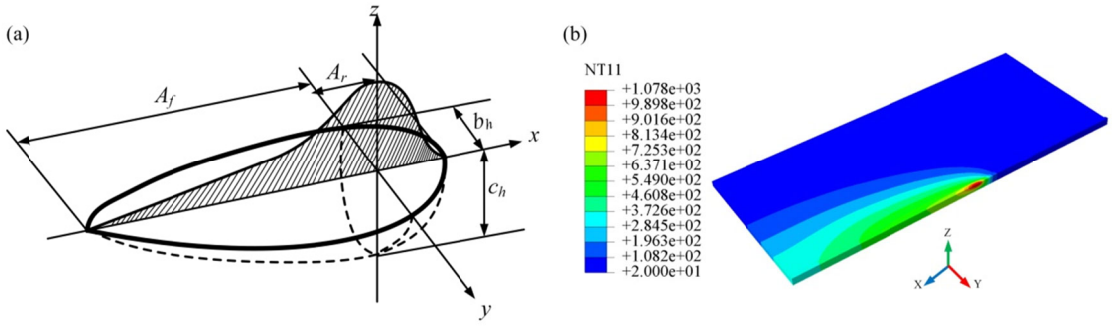

Fig. S8 Heat source model and temperature field diagram during the welding simulation process: (a) Heat source model; (b) Temperature field diagram.

Such a model can more accurately simulate heat distribution during welding, making it particularly well-suited to complex welding processes. In ABAQUS, the double-ellipsoid heat source model is often implemented using the user-defined subroutine DFLUX. The DFLUX subroutine facilitates the definition of heat flux density as a function of position, time, temperature, and other variables. The heat-flux distribution of the double-ellipsoid heat source can be determined using the Fortran code in the DFLUX subroutine.

$$q_f(x,y,z)=\frac{6\sqrt{3}f_fQ}{A_fb_hc_h\pi\sqrt{\pi}}\exp\left(-\frac{3x^2}{A_f^2}-\frac{3y^2}{b_h^2}-\frac{3z^2}{c_h^2}\right) \tag{S12}$$

$$q_r(x,y,z)=\frac{6\sqrt{3}f_rQ}{A_rb_hc_h\pi\sqrt{\pi}}\exp\left(-\frac{3x^2}{A_r^2}-\frac{3y^2}{b_h^2}-\frac{3z^2}{c_h^2}\right) \tag{S13}$$

In the equation, the heat flux densities within the front and rear semi-ellipsoids are represented by q_f and q_r, respectively. The welding heat input is denoted by Q. The lengths of the rear and front semi-axes of the ellipsoids are represented by A_r and A_f, respectively. The width and depth of the heat source are given by b_h and c_h, respectively. The coordinates of the three-dimensional Cartesian system are denoted by x, y, and z. The proportions of heat input to the front and rear semi-ellipsoids are represented by f_f and f_r, respectively, with $f_f+f_r=2$. The parameters of the double ellipsoid heat source are shown in Table S2.

Table S2 Parameters of the double ellipsoid heat source.

Heat source parameters	A_r	A_f	b_h	c_h	f_f	f_r
value	4	7.5	2	2	0.7	1.3

S2.2Material properties and boundary conditions

To enhance computational efficiency, the thermophysical properties of AA5052 aluminum alloy are specified for the simulation model. Key parameters such as density, specific heat capacity, thermal conductivity, and linear expansion coefficient are obtained from the standard material database, and the particular values are presented in Fig. S9 (Xu, 2020). In the numerical simulation, the experimental constraints are reproduced accurately, as illustrated in Fig. S7. Vertical displacement constraints are applied to the corresponding nodes on the upper surface of the model, whilst the three corner points on the bottom surface are fixed with full degrees of freedom. Concurrently, usual constraints are set in the symmetry plane of the model. After simulating the welding process, the constraints on the upper surface are removed in accordance with the test conditions. Thereafter, only the endpoint constraints on the bottom surface and the symmetry-plane constraints are retained to simulate the free deformation state of the workpiece after actual welding.

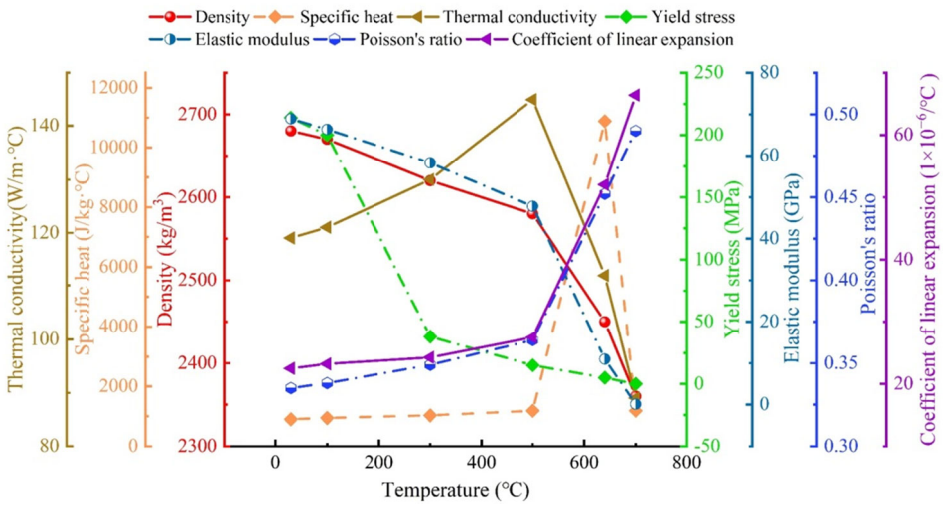

Fig. S9 Material properties at different temperatures.

S2.3 Finite element simulation results and analysis

To investigate the spatial distribution pattern of the temperature field, an array of monitoring points was set up on a transverse datum line 90 mm from the edge of the weldment. Eight characteristic points (labelled A-H) at 0 mm, 1.5 mm, 3 mm, 10 mm, 15 mm, 19 mm, 31 mm, and 42 mm from the edge of the weldment were selected sequentially along this direction, and their spatial distribution is shown in Fig. S10(a).

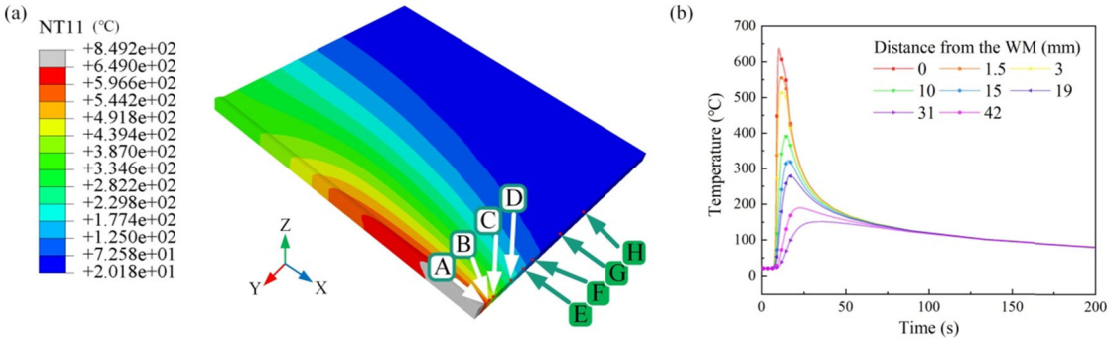

Fig. S10 Cycle profiles at each node: (a) Shape of the temperature melt pool and the location of the take-off point; (b) Thermal cycle profiles corresponding to the take-off point location.

The thermal cycle curve analysis is illustrated in Fig. S10(b). The peak temperature at each monitoring point exhibits a nonlinear decay with increasing distance from the weld. Due to the hysteresis effect in heat conduction, the maximum temperature is significantly delayed in time as one moves farther from the heat source. Given the temperature fluctuations during welding, the entire welded joint is divided into three distinct zones: the WM, HAZ, and BM. The inhomogeneous heating of the HAZ during welding results in substantial differences in its mechanical properties compared to those of the BM .

Establish a coordinate system based on the geometric characteristics of the welded joint, and define the stress components in terms of their orientations. The stress component acting in the direction of weld extension is the longitudinal stress (S11), which is perpendicular to the weld cross-section normal. The stress component perpendicular to the weld direction is named transverse stress (S22), whose direction of action is parallel to the normal vector of the joint cross-section.

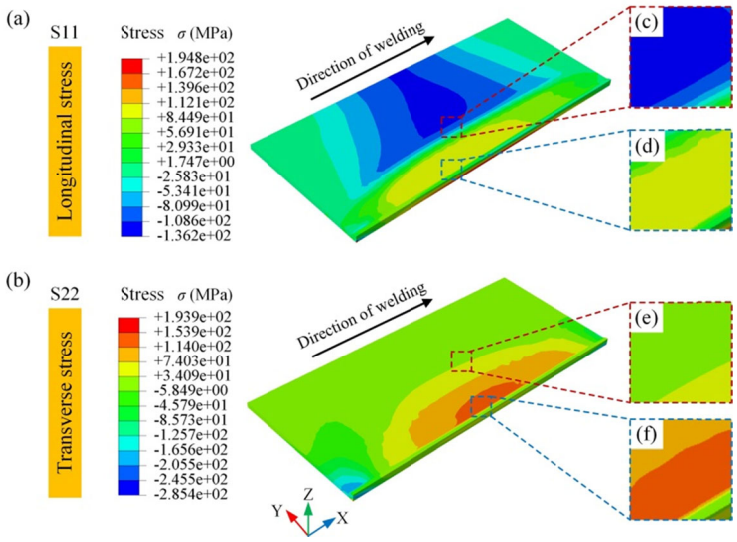

Fig. S11 Cloud view of residual stress distribution during welding simulation of AA5052 aluminum alloy: (a) Longitudinal residual stress S11; (b) S11-BM; (c) S11-HAZ and WM; (d) Transverse residual stress S22; (e) S22-BM; (f) S22-HAZ and WM.

As illustrated in Fig. S11, the distribution characteristics of the residual stress field in AA5052 aluminum alloy welded joints are shown. As shown in Fig. S11(a), significant tensile residual stress concentration is observed in the weld center region, with a peak stress reaching 101.4 MPa. In contrast, the compressive residual stress is primarily distributed in the edge region of the BM, far from the weld seam, forming a pronounced stress gradient. As illustrated in Fig. S11(b), it exhibits a notable degree of regularity in the residual stress distribution within the HAZ and proximity to the center of the weld. The tensile residual stress field, S11, attains a maximum of 120.5 MPa near the weld centerline, then transitions to compressive residual stresses towards the two BM sides. The stress field is symmetrically distributed about the WM of the centerline, exhibiting a mirror-symmetric pattern.

The formation mechanism of this distribution pattern can be attributed to two aspects. Firstly, the non-uniform temperature field of the heat source along the weld direction during the welding process leads to anisotropic thermal expansion of the material. Secondly, during the subsequent cooling process, the solidification shrinkage of the molten pool is constrained by the surrounding solid metal, ultimately resulting in residual tensile stresses in the weld zone and residual compressive stresses in the constraint zone.

As illustrated in Fig. S12(a) and Fig. S12(b), the residual stress distribution along the P1 path in the welded joint of AA5052 aluminum alloy is shown. The finite element calculation results demonstrate strong consistency with the experimental data obtained by the hole-drilling method. Regarding the longitudinal residual stress distribution, a typical cap-shaped pattern is observed along the P1 path. The simulated peak residual tensile stress is 101.3 MPa, while the measured value is 106.4 MPa, with the difference within 5%. This phenomenon is closely related to the thermal cycling characteristics of welding: the central region of the weld undergoes high-temperature thermal expansion during heating, while contraction is restricted during cooling due to temperature gradients. This ultimately results in a significant tensile stress concentration zone forming at the midpoint of the weld(Wang et al., 2022; Lu et al., 2019).

As illustrated in Fig. S12(c) and Fig. S12(d), a comparison is made between the measured and finite-element-predicted residual stresses in AA5052 aluminum alloy welded joints along the P2 path. The analysis results indicate that both transverse S22 and S11 residual stresses along this path exhibit tensile stress states. The spatial distribution of stress values exhibits a significant gradient. Near the center region of the WM, stress concentration occurs. However, because the weld heat source is flush with the BM surface, the stress at the center position exhibits a localized dip. As the distance from the WM center increases, the transverse residual stress decays gradually, approaching the BM of the original stress level.

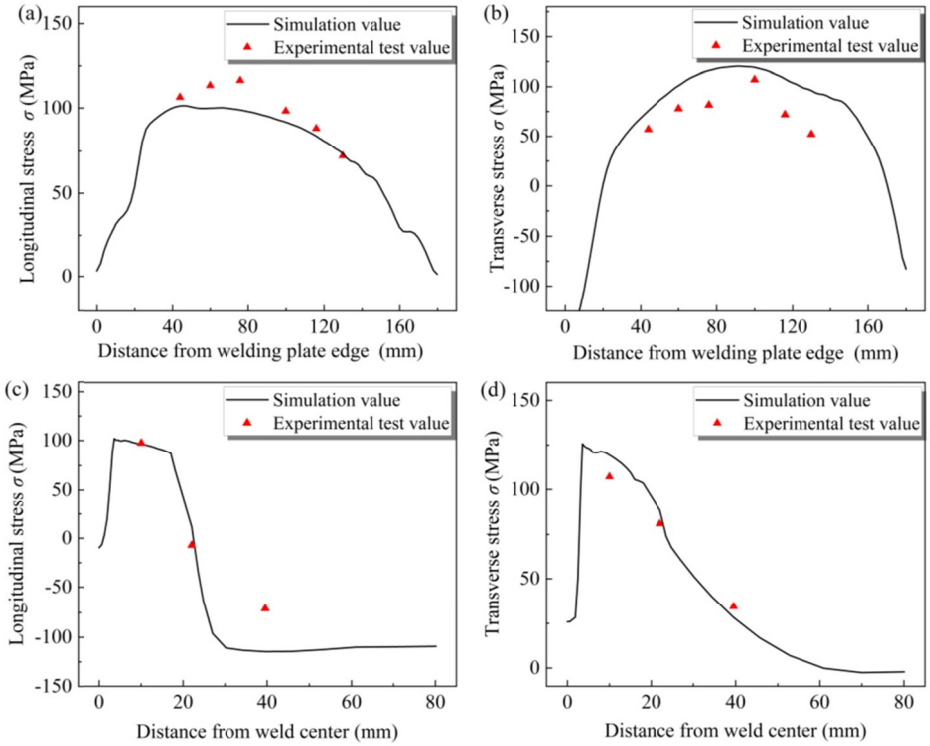

Fig. S12 Residual stress along the paths P1 and P2: (a) P1 longitudinal residual stress; (b) P1 transverse residual stress; (c) P2 longitudinal residual stress; (d) P2 transverse residual stress.

It is noteworthy that a sudden change in stress state occurs approximately 20 mm from the center of the weld. At this point, residual tensile stress transforms into residual compressive stress, reaching its peak at 30 mm. This stress-state transition mechanism is primarily associated with the phase transformation of materials in the HAZ and with the non-uniform contraction behavior during cooling.

The HAZ, defined as the transitional region within welded joints that undergoes complex thermal cycling without melting, exhibits microstructural evolution and residual stress distribution. These phenomena directly determine the service reliability of welded structures. Finite element simulation results indicate that during the welding of AA5052 aluminum alloy, the HAZ experiences significant abnormal grain growth at peak temperatures of 300 ~ 400 °C, resulting in reduced microhardness compared to the base metal. Concurrently, thermo-mechanical coupling simulations reveal pronounced residual tensile stress concentrations at the HAZ edges. The dual effect of microstructural weakening and stress concentration provides a theoretical foundation for predicting subsequent mechanical property test outcomes. In accordance with the Hall-Petch relationship and the coupled effect of stress concentration, it is reasonable to infer that the HAZ will become the preferred fracture zone under tensile loading. To validate these simulation conclusions, a series of standard tensile specimens is designed. The present study will investigate the fracture behavior of the HAZ under quasi-static loading conditions and its intrinsic relationship with the residual stress field. This investigation will entail fracture surface localization and microstructural analysis.

S3 Results

S3.1 Microstructure analysis

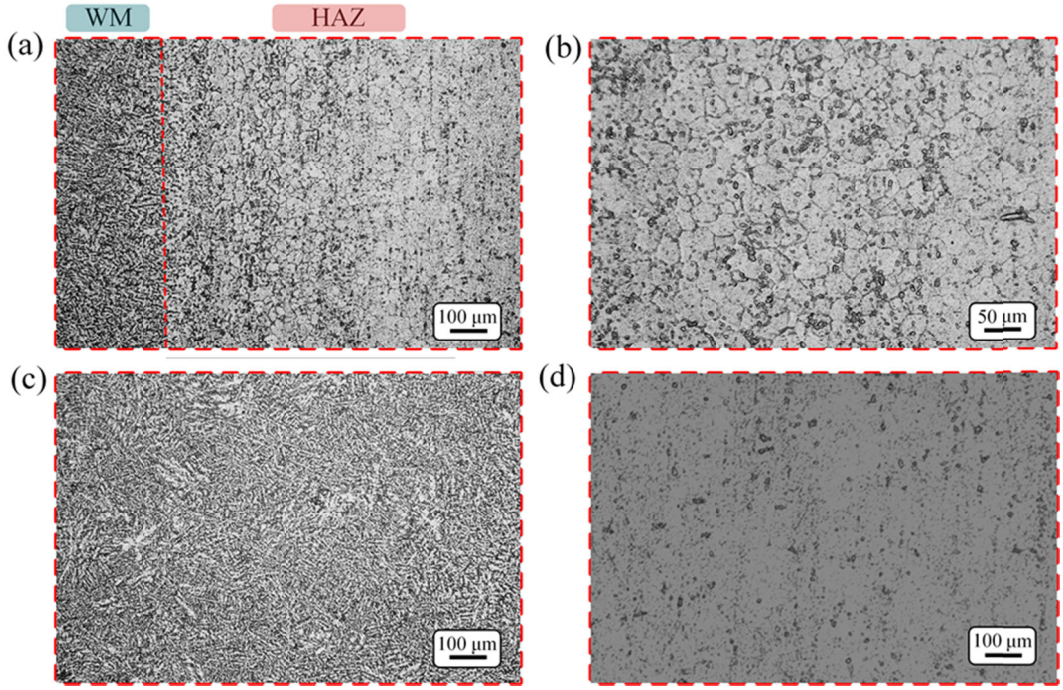

Fig. S13 Metallographic structure of local areas of initial AA5052 aluminum alloy welded joints: (a) Microstructure of WM and HAZ (100 ×); (b) Microstructure of HAZ (200 ×); (c) Microstructure of WM (100 ×); (d) Microstructure of the BM (100 ×).

During welding, the HAZ is heated to high temperatures. However, due to the low melting point and high thermal conductivity of aluminum alloys, a significant heat input is required for welding—the high-temperature effect under investigation results in grain growth in the HAZ and a coarse microstructure. In comparison with the BM aluminum alloy, the WM absorbs a significant amount of heat. It melts during welding, and the weld metal undergoes rapid cooling during solidification. This rapid cooling process has been shown to promote the rapid solidification and crystallization of the WM, leading to grain refinement. Furthermore, the CMT welding method has been observed to exhibit a low heat input, which effectively mitigates overheating in the HAZ. Concurrently, this method promotes rapid WM cooling, thereby achieving grain refinement and homogenization of the WM of the microstructure(Liu et al., 2024; Fu et al., 2025).

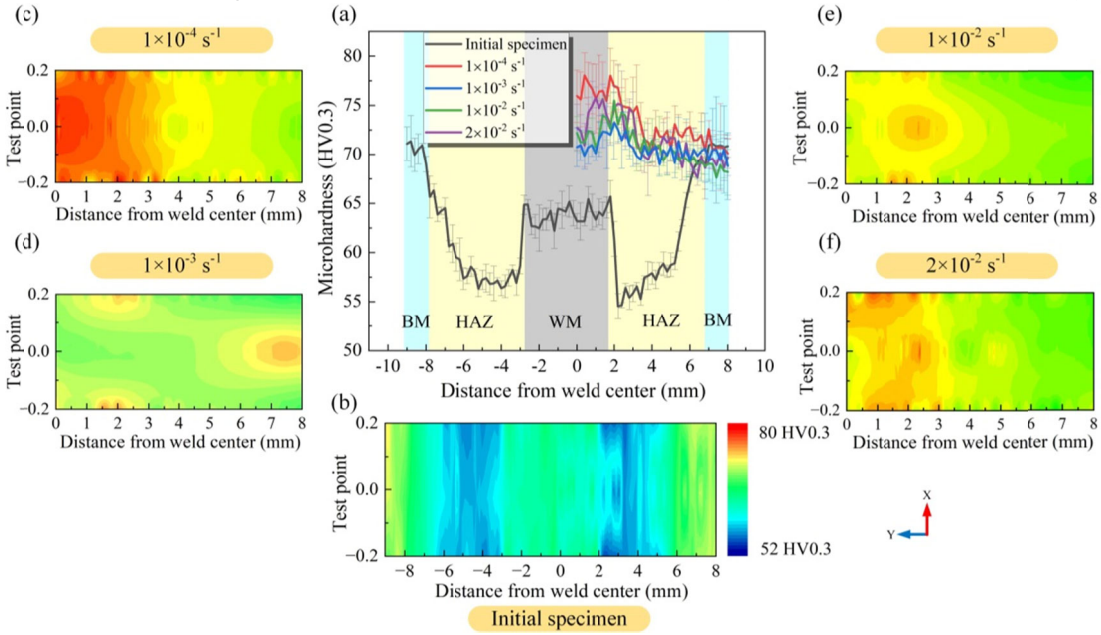

Fig. S14 (a) Microhardness distribution ; (b) Initial specimen microhardness cloud map; (c) $1\times10^{-4}s^{-1}$ specimen microhardness cloud map; (d) $1\times10^{-3}s^{-1}$ specimen microhardness cloud map; (e) $1\times10^{-2}s^{-1}$ specimen microhardness cloud map; (f) $2\times10^{-2}s^{-1}$ specimen microhardness cloud map.

The distribution of microhardness in different characteristic areas of welded joints demonstrates significant non-uniformity. The WM generally exhibits higher microhardness than the BM, a consequence of the melting and solidification processes (Yang et al., 2024). Conversely, the HAZ undergoes a complex phase transformation during the welding thermal cycle, resulting in a gradient of microstructural evolution in this region. This tissue evolution has been shown to result in abrupt changes in microhardness values and to introduce a non-uniform mechanical behavior within the material. According to the results of the surface microhardness gradient tests, the average microhardness values of the different characterized zones show significant differences, with the weld zone microstructure undergoing rapid solidification, resulting in an average microhardness of 63.78 HV0.3. The HAZ, softened by the weld cycle, exhibits a lower average microhardness of 60.15 HV0.3. In contrast, the BM, which constitutes the unaffected original material, maintains the highest average microhardness value of 70.84 HV0.3. After stretching at varying strain rates, the microhardness values of the welded joints were modified.

As shown in Table S3, at a strain rate of 1×10^{-4} s^{-1}, the average microhardness in the weld region was 76.59 HV0.3, with an enhancement rate of 20.08%, while the average microhardness in the HAZ was 72.66 HV0.3, with an enhancement rate of 20.80%. At a strain rate of 1×10^{-2} s^{-1}, the average microhardness in the weld region was 72.51 HV0.3. Enhancement rate of 13.69%. An average microhardness of 70.61 HV0.3 in the HAZ, with an enhancement rate of 17.39%, is reported. At a strain rate of 2×10^{-2} s^{-1}, an average microhardness of 73.93 HV0.3, with an enhancement rate of 15.91% was measured in the weld region. An average microhardness of 70.90 HV0.3 was recorded in the HAZ. Enhancement rate of 17.87%. Furthermore, at a strain rate of 2×10^{-2} s^{-1}, the average microhardness of the BM was found to decrease in comparison to the average microhardness of the unstretched base material. It was lower than the value at a strain rate of 1×10^{-4} s^{-1}, which also occurred at a strain rate of 1×10^{-2} s^{-1}. The work-hardening behavior is more pronounced at lower strain rates, and the material deforms plastically during specimen stretching, thereby increasing dislocation density. The increase in dislocation density hinders subsequent dislocation movement, thereby increasing the material of microhardness (Ma et al., 2014).

Table S3 Comparison of microhardness values of the initial specimen and stretched specimens under different parameters.

Strain rate(s^{-1})	WM(%)	HAZ(%)	BM(%)
Initial specimen	/	/	/
1×10^{-4}	20.08	20.80	-0.41
1×10^{-3}	11.86	17.14	-1.85
1×10^{-2}	13.69	17.39	-3.49
2×10^{-2}	15.91	17.87	-2.70

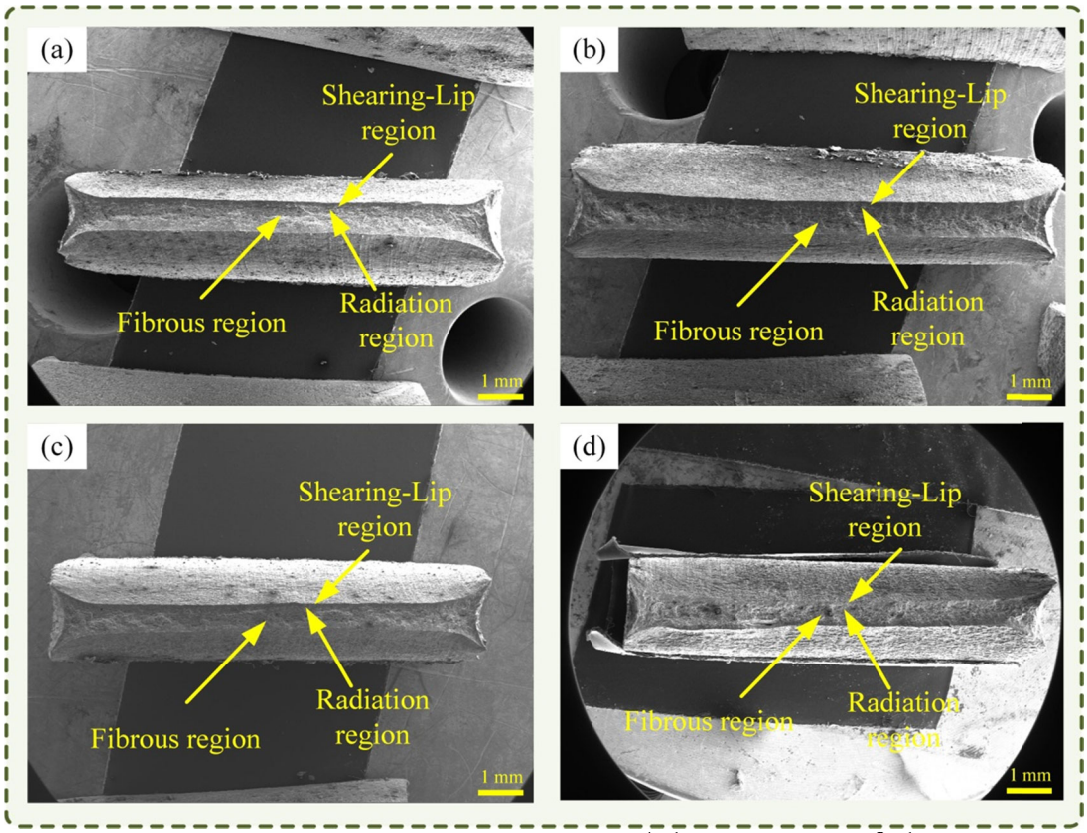

Fig. S15 Macro-morphology of the fracture for each condition: (a) 1×10^{-4} s^{-1} specimen; (b) 1×10^{-3} s^{-1} specimen; (c) 1×10^{-2} s^{-1} specimen; (d) 2×10^{-2} s^{-1} specimen.

As illustrated in Fig. S15, the fracture surface morphology of a rectangular tensile specimen typically exhibits three distinctive regions: the fibrous region, the radiation region, and the shearing-lip region (Li et al., 2025). The fibrous region corresponds to the stage of crack initiation and slow expansion. the radiation region is located in the periphery of the fibrous region, and its radiation prismatic features indicate that the crack is rapidly and unstably expanding in this stage. The shear-lip region, as the final fracture region, and its plastic deformation features reflect the toughness response of the material at the instant of fracture.

As illustrated in Fig. 2, the fracture surface of the original welded joint is characterized by a high density of micro-pores and dimples. This microstructure suggests that the joint follows a micro-pore aggregation-type ductile fracture mechanism (Zhang et al., 2018). The mechanism of dimple formation is closely associated with second-phase particles. During plastic deformation, these hard particles are susceptible to detaching from their interfaces with the aluminum matrix or fracturing internally. This results in the formation of nucleation sites for microvoids. These microvoids subsequently grow and coalesce, ultimately giving rise to the observable dimple morphology. When subjected to external loading, the material initially undergoes plastic deformation. As the loading process continues, microvoids begin to form within the material. These microvoids undergo expansion under sustained loading and ultimately coalesce to form a continuous fracture surface. Dimples, the primary microstructural feature of this fracture mechanism, are essentially microscopic cavities formed during localized plastic deformation of the material. Tensile specimens manifest ductile fracture characteristics under varying strain rates; however, fracture morphology is substantially influenced by strain rate. In ductile materials, the fracture process primarily follows the sequence of void nucleation, coalescence, and growth.

S3.2 The influence of strain rate on the PLC effect

In the context of specific temperature and loading rate conditions, a range of alloy materials manifests a non-uniform plastic destabilization behavior during quasi-static stretching, a phenomenon referred to as the Portevin-Le Chatelier (PLC) effect (Cerny et al., 2024; Xu et al., 2023). This effect manifests in the macroscopic mechanical response through periodic sawtooth-like fluctuations in the stress-strain curve,

accompanied by intermittent evolution of local deformation bands on the specimen surface. When analyzed from a microphysical perspective, the PLC effect can be viewed as a direct reflection of the evolution of the microstructure during material deformation. It has been demonstrated that dynamic strain ageing (DSA) is one of the key factors that induce the PLC effect (Mola et al., 2021). During plastic deformation, solute atoms interact dynamically with moving dislocation, leading to intermittent dislocation motion. This non-uniformity in dislocation dynamics is directly reflected in the jagged fluctuations of the macroscopic stress-strain curve (Magliaro et al., 2025).

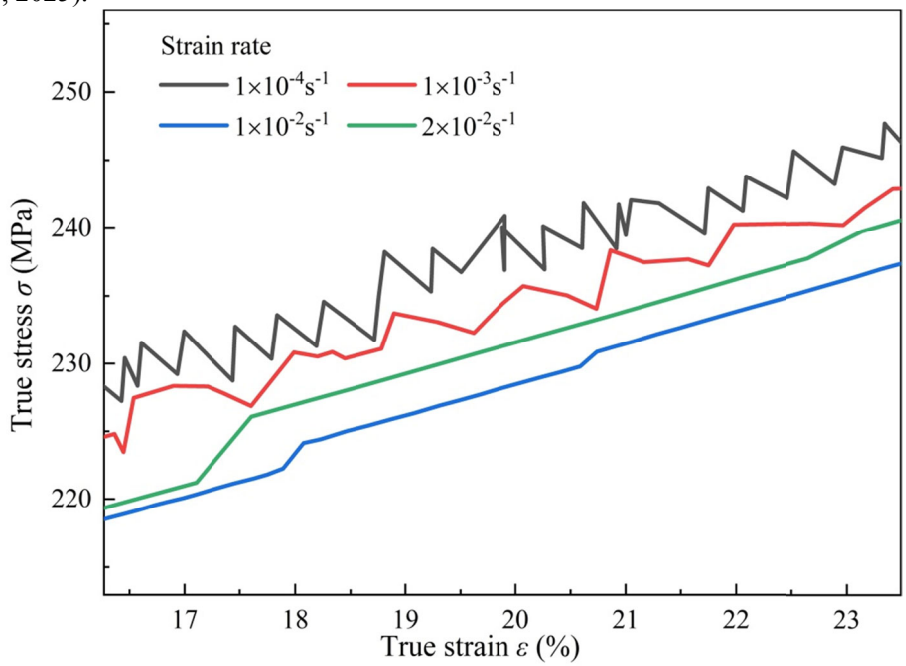

Fig. S16 Stress-strain curves and PLC effects in the HAZ at different strain rates: Stress-strain curves of the HAZ at various strain rates (1×10^{-4} s^{-1}, 1×10^{-3} s^{-1}, 1×10^{-2} s^{-1}, 2×10^{-2} s^{-1}).

It is important to note that the spatial distribution of the PLC effect exhibits a self-organizing characteristic, as demonstrated in Fig. S16.

S3.3 Local strain distribution in welded joints at different strain rates

The distribution of points obtained for the DIC experiment is illustrated in Fig. S17. These points were collected from the WM, HAZ, and BM. Select three points from each area to form a duplicate group. As shown in Fig. S18, the mechanical response characteristics of the welded joints are observed along the longitudinal monitoring path under various strain rate conditions. This figure shows the non-uniform mechanical behavior of the joints during deformation, as revealed by the strain-time response curves (Patil et al., 2025; Su et al., 2021). The analysis of the results demonstrates that the longitudinal strain and stress distributions of the welded specimen exhibit significant spatial gradients. It was further observed that the strain field on both sides of the weld remained approximately symmetrically distributed before fracture. Yet, essential differences in the deformation evolution were evident in different characteristic regions. The BM exhibited the least deformation, followed by the WM, while the HAZ showed the most pronounced strain concentration. This non-uniformity in strain distribution not only reflects the variability in the local mechanical properties of the joint but also suggests that the HAZ may become a critical region for deformation localization, exerting a decisive influence on the failure mode of the overall structure.

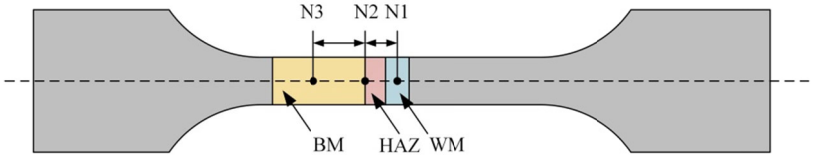

Fig. S17 DIC experimental pickup point layout.

As illustrated in Fig. S17, the method for defining the HAZ involves combining three techniques: tensile

specimen fracture position analysis, microstructure observation, and microhardness testing. Taking the center of the WM as the reference point, a ±4 mm range is defined as the WM zone, the tissue region formed by the solidification of the molten BM mixed with the filler metal during the welding process. The range of ±8 mm or more is defined as the BM. In this area, the material maintains the microstructure and mechanical properties of the original processing state. Between the WM and the BM, the HAZ is subject to significant changes in microstructure and mechanical properties due to the welding thermal cycling process. These changes render it a typical weak link region in welded joints.

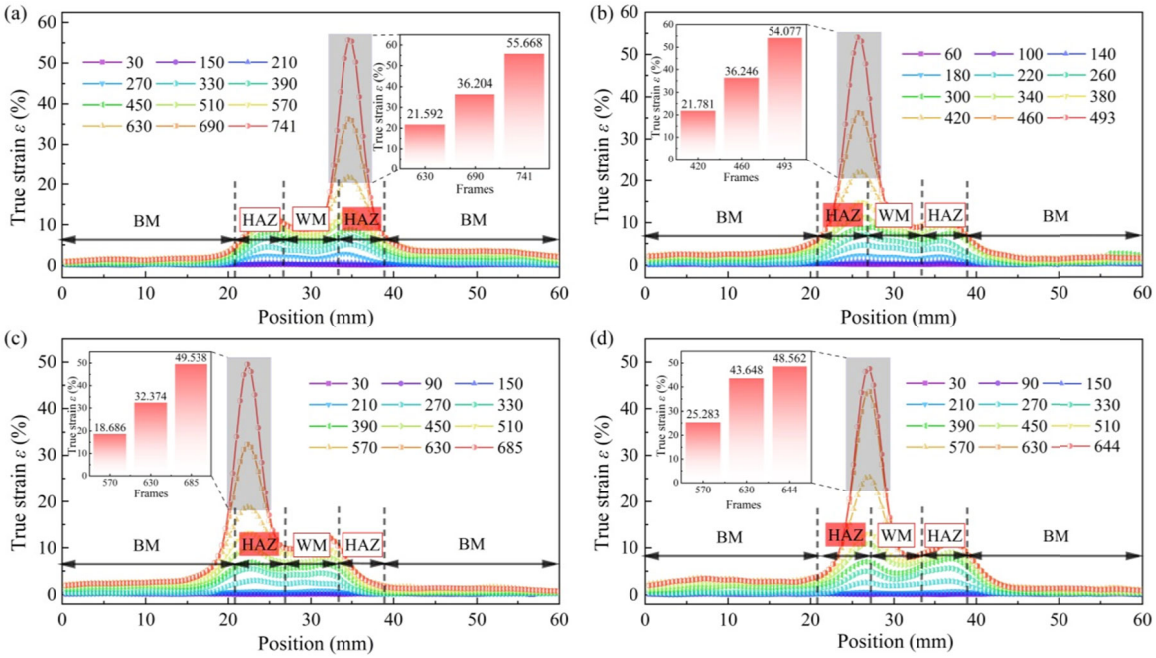

Fig. S18 Strain distribution clouds of specimens at different strain rates: (a) 1×10^{-4} s^{-1} specimen; (b) 1×10^{-3} s^{-1} specimen; (c) 1×10^{-2} s^{-1} specimen; (d) 2×10^{-2} s^{-1} specimen.

As illustrated in Fig. 3, the mechanical behavior of the welded joint in different characteristic areas is analysed. Use DIC technology, and characteristic points are established in the WM, BM, and HAZ for local performance characterization. The true stress-strain response curves for each region can be derived by combining theoretical calculations with the aforementioned DIC technology. The analysis results demonstrate that the true stress-strain curves of different characteristic regions exhibit significant differences in the key deformation stages (e.g., the plastic flow stage), especially at key nodes such as N1, N2, and N3. The DIC technique can discern the mechanical behavior of the materials under investigation. This observation suggests that the DIC technique demonstrates high proficiency in discriminating material heterogeneity and can effectively capture the mechanical properties of local regions within welded joints.

S3.4 The influence of different strain rates on the local properties of welded joints

Fig. 4 presents the fitted stress-strain curves for tensile specimens under four distinct process parameters, demonstrating close alignment with the DIC curves. As shown in Fig. 4 and Fig. S19, and Table 2, the average σ_t of the BM region in specimens tested at strain rates of 1×10^{-2} s^{-1}, 1×10^{-3} s^{-1}, and 1×10^{-4} s^{-1} exhibited an increase of 1.95%, 4.23%, and 8.46%, respectively, in comparison to specimens tested at a strain rate of 2×10^{-2} s^{-1}. Concurrently, the average σ_s increased by 2.61%, 4.87%, and 8.47%, respectively. The findings suggest that as the strain rate diminishes, both the average ultimate strength and average σ_s in the parent material region are augmented.

As demonstrated in Fig. 4, Fig. S19, and Table 2, the average σ_t and σ_s of the HAZ specimens at a strain rate of 1×10^{-2} s^{-1} exhibited an increase of 0.65% and 12.35%, respectively, in comparison to specimens at 2×10^{-2} s^{-1}. As the strain rate decreased to 1×10^{-3} s^{-1}, the average σ_t and σ_s of the specimen HAZ increased by 2.53% and 16.38%, respectively, compared to the specimens at 2×10^{-2} s^{-1}. At a strain rate of 1×10^{-4} s^{-1}, the average σ_t and σ_s of the specimen HAZ increased by 4.30% and 19.39%, respectively, compared to the 2×10^{-2}

s^{-1} specimen. The findings suggest that both the average σ_t and the average σ_s of the HAZ increased as the strain rate decreased.

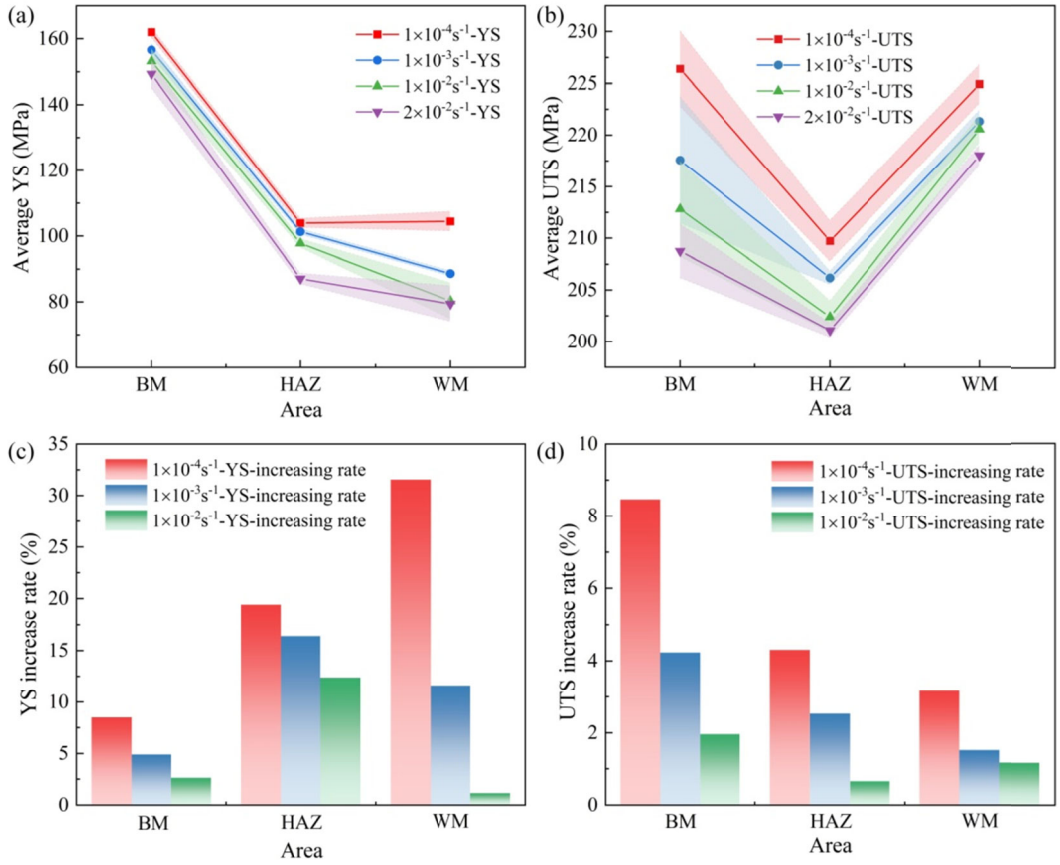

Fig. S19 Local mechanical properties with different parameters: (a) average σ_s; (b) average σ_t; (c) σ_s enhancement ratio; (d) σ_t enhancement ratio.

As demonstrated in Fig. 4 and Fig. S19, and Table 2, for the specimens under a strain rate of 1×10^{-2} s^{-1}, the average σ_t and σ_s of the WM of the specimens were 1.16% and 1.11% higher than those of the specimens in the 2×10^{-2} s^{-1} state.

As the strain rate changed to 1×10^{-3} s^{-1}, there was an observed increase in the average σ_t and σ_s of specimen WM by 1.51% and 11.58%, respectively, in comparison to the initial state specimen at 2×10^{-2} s^{-1}. At a strain rate of 1×10^{-4} s^{-1}, the average σ_t and σ_s of specimen WM increased by 3.16% and 31.54%, respectively, compared to the specimen at 2×10^{-2} s^{-1}. The findings suggest that both the average ultimate strength and the average σ_s in the weld zone increased as the strain rate decreased.

It can be observed that varying degrees of enhancement are achieved in the σ_t and σ_s of each region with the reduction of strain rate. In comparison to the condition with a strain rate of 2×10^{-2} s^{-1}, the most significant effect is achieved under the parameters of 1×10^{-4} s^{-1}, as shown in Fig. S19(a) and (c). WM improvement is the most notable, with an improvement rate of 31.54%, and the order is WM ＞ HAZ ＞ BM. As for the improvement effect of σ_t in each region under various parameters, as shown in Fig. S19(b) and (d), the slowest strain rate also leads to the best improvement effect, with BM showing the most significant enhancement, with an improvement rate of 8.46 %, and the order is BM ＞ HAZ ＞ WM.

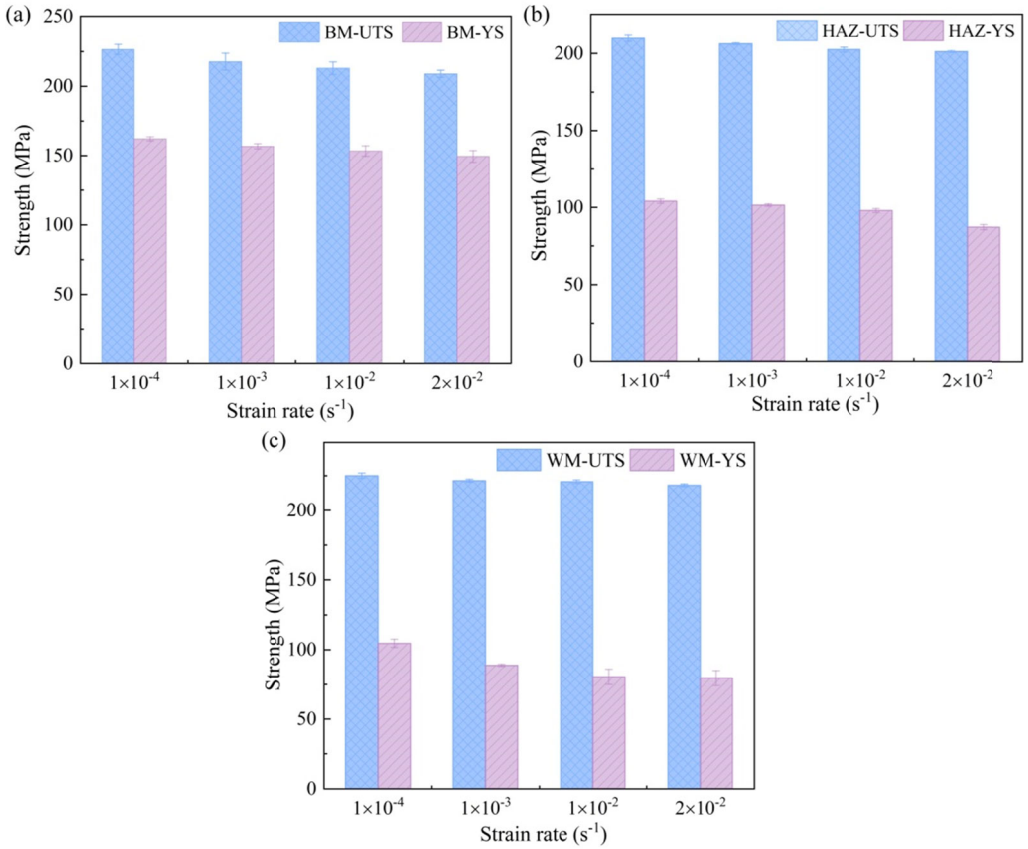

Fig. S20 Average σ_t and average σ_s in different regions: (a) BM; (b) HAZ; (c) WM.

A comparison of the strength enhancement effect in the local area of welded joints reveals that the σ_s enhancement effect is more pronounced than the tensile strength enhancement effect. The *n*-value, a pivotal parameter in the material ontological relationship, quantitatively describes the average evolution law of strain hardening of the material during the stage of homogeneous plastic deformation. Additionally, it profoundly reflects the material of capacity to resist sustained plastic deformation. From a physical perspective, the *n*-value indicates the efficiency of dislocation structure evolution during material deformation. A higher *n*-value is indicative of accelerated dislocation accumulation, more comprehensive grain orientation adjustment, and a more pronounced hardening effect. Work hardening results from increased dislocation density and its interaction with barriers, such as grain boundaries, leading to a continuous increase in deformation resistance. Materials with high *n*-values demonstrate the capacity to undergo uniform deformation over extended periods, thereby enhancing their forming limits and energy absorption capacity.

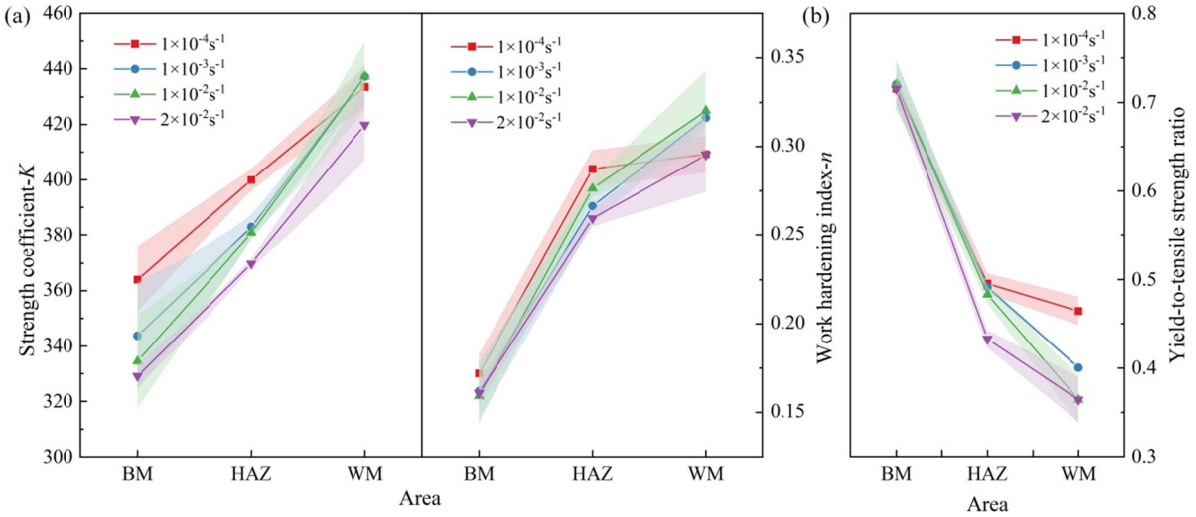

Fig. S21 Localized intrinsic parameters for different strain rate parameters: (a) *K*, and *n*; (b) yield-to-tensile strength ratio.

As shown in Fig. S21(a), the experimental data exhibit a gradual increase from the BM to the WM across different strain rates, as indicated by the processing *n*. Specifically, the index attains its minimum in the BM, increases progressively towards the WM, and reaches its maximum in the WM. In the BM and HAZ regions, *n* shows a slight downward trend with increasing strain rate. Conversely, within the WM, the strain rate has been observed to initially increase the *n* value, but at elevated strain rates (1×10^{-2} s^{-1} and 2×10^{-2} s^{-1}), a slight decrease has been documented. According to the dynamic strain-aging theory, the variation in *n* is influenced by the interaction between solute atoms and dislocation. At low strain rates, sufficient time is provided for solute atoms to diffuse and interact with dislocation, thereby enhancing the material of strain-hardening capacity. However, when the strain rate is excessively high, the diffusion of solute atoms is unable to keep pace with the movement of dislocation. This leads to weakening of the dynamic strain-aging effect, and a subsequent decrease in the *n* value results.

As shown in Fig. S21(a), the experimental data indicate that the *K* of the welded joint exhibits significant spatial variations under different strain rates. Specifically, the gradient increase from the BM to the WM is presented by the coefficient, with the BM having the lowest value and the WM reaching the peak. It is noteworthy that the *K* in the BM and the HAZ demonstrates sensitivity to strain rate changes, exhibiting a slight downward trend as the strain rate increases. This strain rate dependency suggests the involvement of time-dependent plastic deformation processes in the deformation mechanism of these regions. In the WM, the *K* value demonstrates an initial increase with the strain rate, subsequently decreasing marginally at elevated strain rates (1×10^{-2} s^{-1} and 2×10^{-2} s^{-1}). The *K*, which is indicative of the material of initial strength, is associated with the dislocation density and solute atom concentration of the material, as stipulated by the Hollomon equation. At low strain rates, the dislocation density is increased by the strong interaction between solute atoms and dislocation, and thus, the *K* value is increased. However, when the strain rate is excessively high, the dislocation density is reduced by insufficient solute atom diffusion and relatively free dislocation movement, thereby diminishing the *K* value.

As illustrated in Fig. S21(b), trends in the yield-to-tensile strength ratio across distinct welded joint regions at varying strain rates are evident. In the BM, HAZ, and WM, a ratio of an initial increase to a subsequent slight decrease is observed with increasing strain rate. The yield-to-tensile strength ratio is indicative of the uniform deformation capacity of the material. At low strain rates, the uniform deformation capacity of the material is enhanced by the strong interaction between solute atoms and dislocation. However, at elevated strain rates, the capacity of the material to undergo uniform deformation is diminished due to inadequate solute atom diffusion and localized deformation.

A combination of Fig. S13 and Fig. S21 demonstrates that the distinct microstructures in the BM, HAZ, and WM regions give rise to disparate dislocation motion mechanisms and DSA effects at varying strain rates, thereby resulting in varied strain rate sensitivities. The elevated grain boundary density in the WM region has been shown to impede dislocation motion more effectively, thereby affording additional time for solute atom diffusion and, consequently, amplifying the DSA effect (Chávez et al., 2020). DSA is defined as alterations in material mechanical properties that result from the dynamic interaction between solute atoms and dislocation. At lower strain rates, dislocation motion is slow, allowing solute atoms sufficient time to diffuse and form solute environments with dislocation. This hinders dislocation movement, enhancing the work-hardening capacity and strength of the material. However, when strain rates become excessively high, solute atom diffusion cannot keep pace with dislocation motion. Consequently, the dynamic strain aging effect weakens, leading to decreases in *n* and *K*.

S3.5 The influence of different strain rates on the work hardening rate.

After the yield stage, the plastic deformation of a material must be sustained by stress enhancement, a phenomenon known as strain hardening. In this stage, the strain-hardening capability of a material can be characterized by the stress at a given strain, and a higher stress indicates a stronger hardening effect. In order to investigate the effect of different strain rates on the hardening behavior of the material, the true stress-strain curve combined with the K-M model was used to characterize the strain hardening properties of the material by calculating the instantaneous hardening rate parameter. This alytical method involves the derivation of the true σ-ε curve, and the results are shown in Fig. S22.

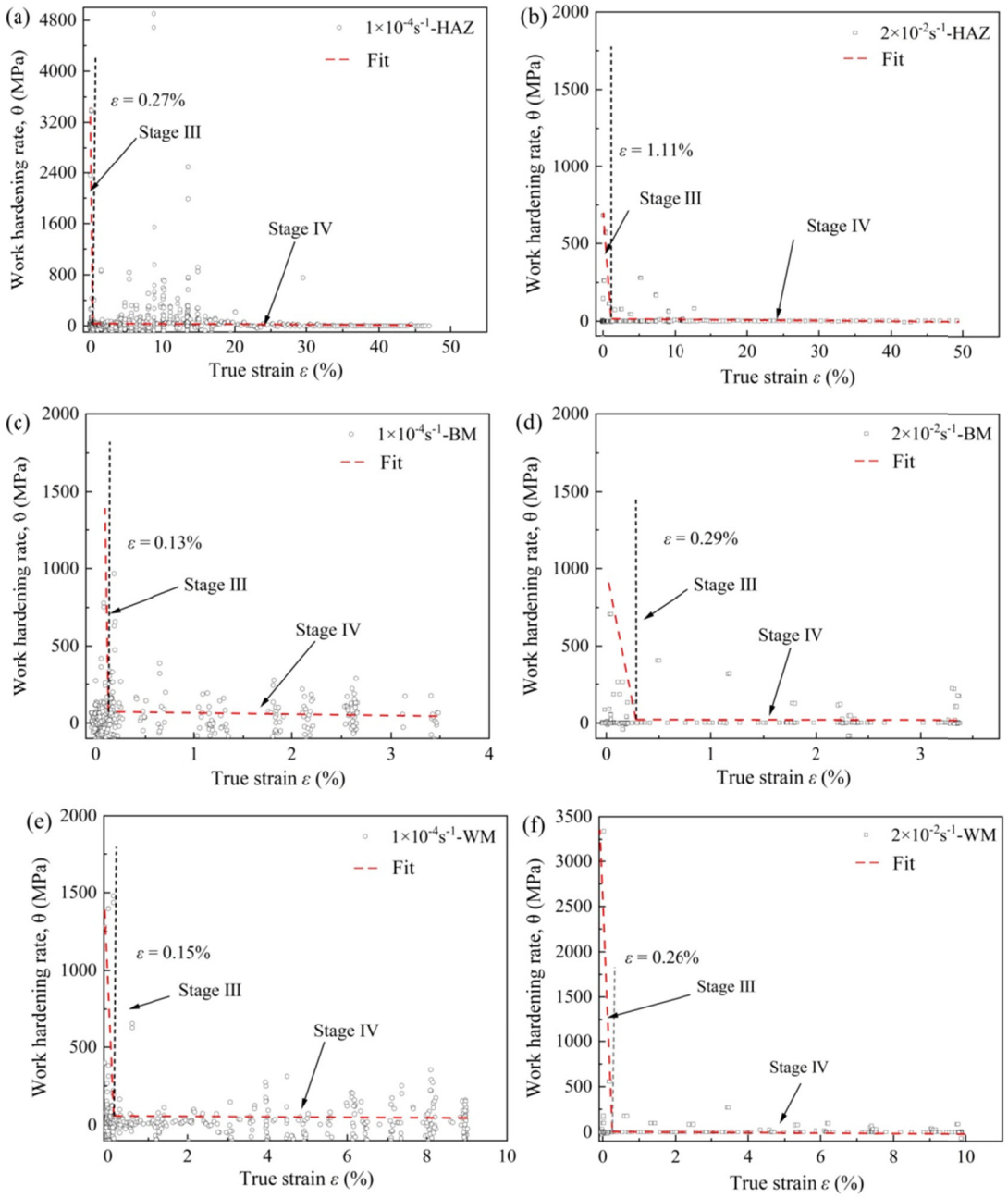

Fig. S22 Strain hardening rates: (a) 1×10^{-4} s^{-1}-HAZ; (b) 2×10^{-2} s^{-1}-HAZ; (c) 1×10^{-4} s^{-1}-BM; (d) 2×10^{-2} s^{-1}-BM; (e) 1×10^{-4} s^{-1}-WM; (f) 2×10^{-2} s^{-1}-WM.

To investigate the impact of strain rate on local strain hardening behavior, strain rates of 1×10^{-4} s^{-1} and 2×10^{-2} s^{-1} were employed. The entire tensile process was divided into the initial hardening stage (Stage Ⅲ) and the strain hardening stage (Stage Ⅳ). As shown in Fig. S22(a) and Fig. S22(b), at a strain rate of 1×10-4 s-1, the stage transition point in the HAZ of the specimen was 0.27%. When the strain rate increased to 2×10^{-2} s^{-1}, the stage transition point shifted to 1.11%. Additionally, when ε exceeded 1%, the strain hardening rate in the HAZ tended to level off.

As shown in Fig. S22(c) and Fig. S22(d), at a strain rate of 1×10^{-4} s^{-1}, the BM undergoes work hardening at $\varepsilon > 0.13\%$. The onset of the work-hardening stage shifts to $\varepsilon > 0.29\%$ when the strain rate increases to 2×10^{-2} s^{-1}. As shown in Fig. S22(e) and Fig. S22(f), at a strain rate of 1×10^{-4} s^{-1}, the phase transition point for the WM was 0.15%. The phase transition point for the WM shifted to 0.26% when the strain rate increased to 2×10^{-2} s^{-1}. The strain rate exerted the most significant influence on the strain-hardening rate in the HAZ. The WM and BM regions of the AA5052 aluminum alloy welded joint exhibited greater hardening capacity than

the HAZ at both strain rates tested. Slower strain rates yielded superior strain hardening capability.

References

Basan R, Franulović M, Prebil I, et al., 2017. Study on Ramberg-Osgood and Chaboche models for 42CrMo4 steel and some approximations. *Journal Of Constructional Steel Research*, 136:65–74. https://doi.org/10.1016/j.jcsr.2017.05.010

Cerny A, Grabner F, Arnoldt AR, et al., 2024. Mechanisms of electrically assisted deformation of an Al–Mg alloy (AA5083-H111): Portevin–Le Chatelier phenotype transformation, suppression, and prolonged necking. *Materials Science And Engineering: A*, 910:146865. https://doi.org/10.1016/j.msea.2024.146865

Chávez BW, Garcés G, Pérez P, et al., 2020. Envejecimiento dinámico por deformación en aleaciones Mg-Gd solubilizadas ensayadas a compresión a temperaturas intermedias. *Revista de Metalurgia*, 56(3):e175. https://doi.org/10.3989/revmetalm.175

Fu NN, Guo D, Ding YP, et al., 2025. Microstructure and mechanical properties of stationary shoulder stir friction welded joints of 6005A-T6 aluminum alloy sections. *Metal Forming*, (05):76–83. https://link.cnki.net/urlid/11.5627.TH.20250124.0923.002

GB/T 31310-2014, 2014. Metallic material: determination of residual stress: hole drilling strain-gauge method. Beijing: Standards Press of China.

GB/T 228.1-2021, 2021. Metallic Materials-Tensile Testing-Part 1: Method of Test at Room Temperature. Beijing: Standards Press of China.

Gu BP, Zhuo JS, Xu GH, et al., 2025. Study on the effects of ultrasonic impact treatment on the local mechanical properties of welded joints based on the digital image correlation. *Measurement*, 239:115441. https://doi.org/10.1016/j.measurement.2024.115441

Kang SK, Kim YC, Kim KH, et al., 2014. Constitutive equations optimized for determining strengths of metallic alloys. *Mechanics of Materials*, 73:51-57. https://doi.org/10.1016/j.mechmat.2014.01.010

Liu Y, Wu DT, Gao ZH, et al., 2024c. Influence of cold metal transfer welding parameters on the welding hot crack of Mar-M247 nickel-based superalloy. *Journal Of Materials Research And Technology*, 30:6341–6354. https://doi.org/10.1016/j.jmrt.2024.05.061

Lu YH, Zhu SC, Zhao ZT, et al., 2019. Numerical simulation of residual stresses in aluminum alloy welded joints. *Journal Of Manufacturing Processes*, 50:380–393. https://doi.org/10.1016/j.jmapro.2019.12.056

Leitão C, Galvão I, Leal RM, et al., 2012. Determination of local constitutive properties of aluminium friction stir welds using digital image correlation. *Materials & Design*, 33:69–74. https://doi.org/10.1016/j.matdes.2011.07.009

Ma HJ, Huang L, Tian Y, et al., 2014. Effects of strain rate on dynamic mechanical behavior and microstructure evolution of 5A02-O aluminum alloy. *Materials Science And Engineering: A*, 606:233–239. https://doi.org/10.1016/j.msea.2014.03.081

Mola J, Luan GQ, Huang QL, et al., 2021. Dynamic strain aging mechanisms in a metastable austenitic stainless steel. *Acta Materialia*, 212:116888. https://doi.org/10.1016/j.actamat.2021.116888

Magliaro J, Behtash AMK, Alpas AT, 2025. Formability limits and fracture mechanisms in AA5182 Al-Mg sheets under room and cryogenic temperature conditions. *Materials Science And Engineering: A*, 936:148388. https://doi.org/10.1016/j.msea.2025.148388

Peng Y, Wu C, Gan JL, et al., 2018. Determination of the local constitutive properties of the welded steel joints using digital image correlation method. *Construction And Building Materials*, 171:485–492. https://doi.org/10.1016/j.conbuildmat.2018.03.182

Patwardhan PS, Nalavde RA, Kujawski D, 2019. An Estimation of Ramberg-Osgood Constants for Materials with and without Luder's Strain Using Yield and Ultimate Strengths. *Procedia Structural Integrity*,

17:750–757.
https://doi.org/10.1016/j.prostr.2019.08.100

Patil SA, Jha A, Ganesh PS, et al., 2025. A study on laser welding of Inconel 718 and evolution of strain field using digital image correlation to estimate the localized properties. *Optics And Laser Technology*, 184:112472.
https://doi.org/10.1016/j.optlastec.2025.112472

Su LH, Fei ZY, Davis B, et al., 2021. Digital image correlation study on tensile properties of high strength quenched and tempered steel weld joints prepared by K-TIG and GMAW. *Materials Science And Engineering: A*, 827:142033.
https://doi.org/10.1016/j.msea.2021.142033

Wang JN, Chen X, Yang LF, et al., 2022. Sequentially combined thermo-mechanical and mechanical simulation of double-pulse MIG welding of 6061-T6 aluminum alloy sheets. *Journal Of Manufacturing Processes*, 77:616–631.
https://doi.org/10.1016/j.jmapro.2022.03.046

Xu JB, Hopperstad OS, Holmedal B, et al., 2023. On the spatio-temporal characteristics of the Portevin-Le Chatelier effect in aluminium alloy AA5182: An experimental and numerical study. *International Journal Of Plasticity*, 169:103706.
https://doi.org/10.1016/j.ijplas.2023.103706

Xu X., 2020. Finite Element Analysis of CMT Welding Process of Aluminum Alloy Sheet. Nanchang University, Nanchang, China.
https://link.cnki.net/doi/10.27232/d.cnki.gnchu.2022.002677

Ye J, Yang RX, Liu YY, et al., 2025. Stress-strain characterization of wire and arc additively manufactured aluminium alloys using the Ramberg-Osgood model. *Journal of Building Engineering*, 105:112519.
https://doi.org/10.1016/j.jobe.2025.112519

Yang SH, Yang XY, Lu X, et al., 2023. Strength calculation and microstructure characterization of HAZ softening area in 6082-T6 aluminum alloy CMT welded joints. *Materials Today Communications*, 37:107077.
https://doi.org/10.1016/j.mtcomm.2023.107077

Zhang WL, Chen XF, Zhuo BC, et al., 2018. Effect of strain rate and temperature on dynamic mechanical behavior and microstructure evolution of ultra-high strength aluminum alloy. *Materials Science And Engineering: A*, 730:336–344.
https://doi.org/10.1016/j.msea.2018.06.018